Various defect states in *a*-Si:H studied by modulated photoconductivity spectroscopy

P. Kounavis*
Department of Engineering Sciences, School of Engineering, University of Patras, 26500 Patra, Greece
(Received 9 August 2001; revised manuscript received 19 October 2001; published 4 April 2002)

Various kinds of defect state distributions dominating electron trapping and recombination in *a*-Si:H films from different laboratories are studied by analyzing modulated photocurrent measurements obtained by varying the frequency or the bias light level. The characteristic features of the experimental modulated photocurrent spectra are compared with those predicted theoretically and a clear physical meaning is obtained. Two kinds of defect states are extracted directly from the spectra without prior assumptions about the form of the density of states. The energetic distributions of these defect states at the quasi-Fermi level and above it are calculated and their magnitude was found to differ by about an order of magnitude, while their capture coefficients differ by as much as 2–3 orders of magnitude. We assign the two kinds of defects to silicon dangling bonds with three backbonded silicon atoms and silicon dangling bonds where one backbond is substituted by hydrogen.

DOI: 10.1103/PhysRevB.65.155207 PACS number(s): 61.72.Hh, 81.15.Ef, 73.50.Gr, 71.55.Jv

I. INTRODUCTION

The determination of the energetic distribution and the nature of the defect states that dominate trapping and recombination of free carriers is of crucial importance in understanding the optoelectronic properties of *a*-Si:H. After many years of intensive research there is now a considerable evidence that the dominant defect states in *a*-Si:H originate from the Si dangling bonds that are charged or neutral. The defect state distribution depends on the material composition, preparation conditions, and after deposition treatment such as light irradiation, electron bombardment, thermal annealing, etc.

The defect pool model is the current prevailing model that describes the formation and equilibration of the dangling bonds.[1–3] According to this model, the density of states (DOS) distribution in the energy gap consists of positively (D^+), negatively (D^-) charged, and neutral (D^0) dangling bonds above, below, and near midgap, respectively. Their relative density is strongly determined from the position of the Fermi level.

Various experiments have been developed to determine the defect state distribution of *a*-Si:H and to compare it with that predicted theoretically. However, each experiment is not necessarily sensitive to the same kind of defects. For example, dark and light induced electron spin resonance experiments[4,5] provide the density of neutral defects and the total density of neutral plus charged defects respectively, while other experiments based on optical absorption,[6–8] capacitance,[9] steady state,[10,11] and transient[13,12] photoconductivity measurements provide mixed combinations of neutral and charged defect densities. Thus different experimental techniques must be combined to obtain a comprehensive picture of the DOS.

The modulated photocurrent (MPC) experiment is widely used as a simple and powerful tool to determine the unoccupied DOS distribution of amorphous semiconductors.[14–18] The absolute DOS is extracted usually assuming that only a single kind of gap states is probed. However, this experiment provides, in general, the summation of all the different kinds of defect states, with which the majority carriers interact, multiplied by their capture coefficient. Therefore it is required to develop analytical techniques which should be able to resolve the different kinds of defects and to clarify their character. To this end, an improved analysis of the MPC was proposed recently[19] which provides important information about the DOS of different kinds of defects that could not be obtained from the previous analyses. This analysis is applied here to experimental MPC spectra of an undoped *a*-Si:H film. In order to obtain a more general validity of the calculated DOS of *a*-Si:H, experimental MPC spectra of undoped samples from different laboratories[20–22] that have been measured by varying the frequency or the bias light level have been selected from the literature to be analyzed as well. Contributions from two kinds of defect states are resolved directly from the experimental spectra of all the samples without prior assumptions about the form of the DOS. The unoccupied and the partially occupied DOS of each kind of defects at the quasi-Fermi level and above it are calculated by means of phase shift and amplitude of the MPC measurements. The capture coefficients of the probing defect states are extracted, from which information about their character is deduced.

II. SAMPLES AND MEASUREMENTS

The *a*-Si:H film, referred to as sample 1, has been deposited on a Corning glass substrate at a temperature $T_s = 300\,^{\circ}\mathrm{C}$ by the rf glow discharge technique using pure silane of a pressure of 100 mTorr in an ultrahigh vaccum chamber. The base vaccum before deposition was 1×10^{-8} Torr and the film thickness was 0.7 μm. Coplanar Al Ohmic contacts with 0.15 mm separation were evaporated on the top of the film and a voltage of 100 V was applied for the photocurrent measurements.

In the MPC experiment the sample was illuminated with a relatively weak sinusoidally modulated light imposed on a stronger dc bias illumination produced by two light emitted diodes respectively with a maximum intensity at 660 nm. The resulting phase shift Φ and the amplitude of the MPC i_{ac} were measured by a lock-in amplifier[20,23] as a function of the modulation frequency keeping constant the bias light

level which is known as frequency scan (FRS) spectroscopy.

Our analysis is applied also to previously published experimental MPC spectra of undoped *a*-Si:H films from three different laboratories. The data from two of these samples referred to as samples 2 and 3 of Ref. 20 and Ref. 21, respectively, have been measured with the conventional FRS spectroscopy, while the data from the other sample, referred to as sample 4, of Ref. 22 has been recorded by varying the bias light level, the so called bias light scan (BLS) spectroscopy. All the examined experimental data are referred to near room temperature where it is believed that trap limited transport dominates[24] and in which our model analysis is based.

III. FRS AND BLS SPECTROSCOPES FOR THE DETERMINATION OF DIFFERENT KINDS OF DEFECT DISTRIBUTIONS

Our analysis of the MPC for the determination of different kinds of defect states has been presented in details elsewhere[19] and it was mainly concentrated on data recorded with the FRS spectroscopy. Here this analysis is briefly presented for data obtained from both the FRS and BLS spectroscopes.

The phase shift ϕ and the amplitude i_{ac} of the MPC reflect the interaction of the free majority carriers with the gap states. Assuming that electrons are the majority carriers and interact, in general, with several kinds of defect states labeled by (i) having distributions $D^i(E)$ each with capture coefficients c_n^i and c_p^i for the electrons and holes, respectively, the calculated imaginary Y term of the MPC by means of Φ, i_{ac} data is directly related to these distributions through

$$Y=\mu e G_{ac} A\mathcal{E}\frac{\sin\phi}{\imath_{ac}}\cong\frac{\pi}{2}\sum_i H^i c_n^i D^i(E_b^i)kT. \qquad (1)$$

In this equation, μ is the mobility of the majority carriers, e the electronic charge, G_{ac} the amplitude of the alternative generation rate, A the conduction cross sectional area of the specimen, kT the thermal energy, and $\mathcal{E}$ the applied electric field. Each probing energy level E_b^i is given by

$$E_b^i=kT\ln\left(\frac{c_n^i N_C}{(\omega^2+\{\omega_t^i\}^2)^{1/2}}\right), \qquad (2)$$

where N_C is the density of states in the conduction band edge where the zero of the energy scale is taken. At every transition frequency ω_t^i it is $\omega_t^i=nc_n^i+pc_p^i=r_n^i(E_t^i)$, where n and p is the density of free electrons and holes, respectively, and $r_n^i(E_t^i)$ the thermal emission rate from the respective quasi-Fermi level E_t of trapped electrons. By taking that $n\gg p$ such that $nc_n^i\gg pc_p^i$ then it is $\omega_t^i\cong nc_n^i$. The weighting function H^i in Eq. (1) is given by

$$H^i=1-\frac{2}{\pi}\arctan\left(\frac{\omega_t^i}{\omega}\right), \qquad (3)$$

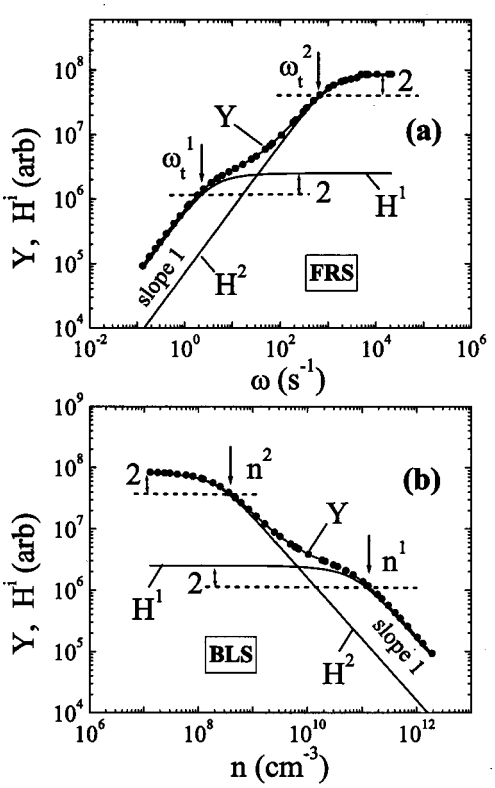

FIG. 1. Calculated values of Y term from Eq. (4) as a function of angular modulation frequency ω for the FRS spectroscopy in (a) and as a function of free electrons concentration n for the BLS spectroscopy in (b). Arrows indicate the characteristic frequencies ω_t^1 and ω_t^2 and the characteristic concentrations n^1 and n^2, while solid lines indicate the variation of the respective weighting functions H^1, H^2.

and determines the individual contribution to the imaginary term of every effective trapping rate $(\tau_b^i)^{-1}=H^i c_n^i D^i(E_b^i)kT$.

For a given temperature, T, Eq. (2) suggests that different gap states can be probed by changing not only the modulation frequency in the conventional FRS spectroscopy, but alternatively the free carriers density with the change of the bias-light level in the BLS spectroscopy.[19] Specifically, in the FRS spectroscopy, every probing energy level E_b^i is shifted from the quasi-Fermi level E_t and above it by scanning in the frequency region of $\omega\geqslant\omega_t^i$ keeping constant the bias light level. In the BLS spectroscopy, every probing energy level E_b^i is shifted along with the respective quasi-Fermi level E_t by scanning with moderate or strong bias light intensities such that $n\geqslant n^i=\omega/c_n^i$, while ω is kept constant. Finally, the E_b^i level remains practically fixed at the respective E_t level for $\omega<\omega_t^i$ and at a fixed energy level above E_t level for $n<n^i$ in FRS and BLS spectroscopy, respectively.

The capture coefficients c_n^i and the defect $D^i(E)$ distributions can be extracted simultaneously from the spectrum of Y term. This is demonstrated with the examples of the calculated spectra of Y term shown in Figs. 1(a) and 1(b) as a function of angular frequency ω and free electrons concentration n for FRS and BLS spectroscopy, respectively. Assuming for simplicity two uniform defect distribut-

ions with $D^1(E)=1\times10^{16}$ cm^{-3} eV^{-1} and $D^2(E)=1\times10^{15}$ cm^{-3} eV^{-1} having $c_n^1=6.3\times10^{-9}$ cm^{-3} s^{-1} and $c_n^2=2.1\times10^{-6}$ cm^{-3} s^{-1}, the Y term is calculated from

$$Y=H^1[\pi/2]c_n^1D^1(E_b^1)kT+H^2[\pi/2]c_n^2D^2(E_b^2)kT. \quad (4)$$

The presence of the two kinds of defects becomes evident in the spectra of Y with the transition to the trapping-limited regime where the effective contribution of each defect vanishes. This transition takes place at two different ω_t^i and two different n^i in the respective spectra of FRS and BLS spectroscopy because of the different capture coefficients of the probing defects. This can be seen in Figs. 1(a) and 1(b), where Y represents two steps by decreasing ω and increasing n, respectively. Each step of Y reflects the decrease of the respective effective trapping rate $(\tau_b^i)^{-1}$ either by shifting each probing level E_b^i close to the quasi-Fermi level E_t upon decreasing ω to ω_t^i or by shifting E_t close to each E_b^i upon increasing n to n^i. The above ''staircaselike'' behavior of Y arises from the decrease of the H^1 and H^2 functions (solid lines) at the respective transition frequencies ω_t^1 and ω_t^2 of Fig. 1(a) and transition concentrations n^1 and n^2 of Fig. 1(b).

In the emission-limited regime that takes place for $\omega\geqslant20\omega_t^i$ and $n\leqslant n^i/20$, it is $H^i=1$ and the spectra represent a leveling off at a value that depends on the absolute probing defect density. Upon decreasing ω and increasing n the trapping-limited regime is obtained for $\omega<\omega_t^i$ and $n>n^i$, respectively, where the H^i and the respective effective trapping rate $(\tau_b^i)^{-1}$ decreases linearly to zero. At every $\omega=\omega_t^i$ and $n=n^i$ of the transition region, H^i has dropped to a factor of 2 from unity (double arrows in Fig. 1). Since at each step of Y the respective effective trapping rate $(\tau_b^i)^{-1}$ dominates the imaginary term, Y drops by a factor of 2 as well and this is used to determine the respective ω_t^i and n^i. Each ratio μ/c_n^i is calculated from

$$\frac{\mu}{c_n^i}\cong\frac{\sigma_{dc}}{e\omega_t^i} \quad (5)$$

and

$$\frac{\mu}{c_n^i}\cong\frac{\sigma_p^i}{e\omega}, \quad (6)$$

where σ_{dc} and σ_p^i are the dc photoconductivities for the bias light intensities corresponding to n and n^i for the FRS and BLS spectroscopy, respectively. By incorporating each ratio μ/c_n^i in Eq. (1) the respective $D^i(E)$ distributions are obtained from the MPC data for $\omega\geqslant\omega_t^i$ and $n\geqslant n^i$.

IV. EXPERIMENTAL RESULTS

Experimental spectra of MPC amplitude i_{ac}, phase shift Φ, and out of phase MPC amplitude $i_{\rm out}$ from FRS spectroscopy at 297 K of our sample 1 are shown as a function of the angular modulation frequency ω in the graphs (a), (b), and (c), respectively, of Fig. 2 for two bias light levels. In the above figures a crossing effect in the spectra of Φ and i_{ac} is observed which appears as a common characteristic of all the *a*-Si:H samples.

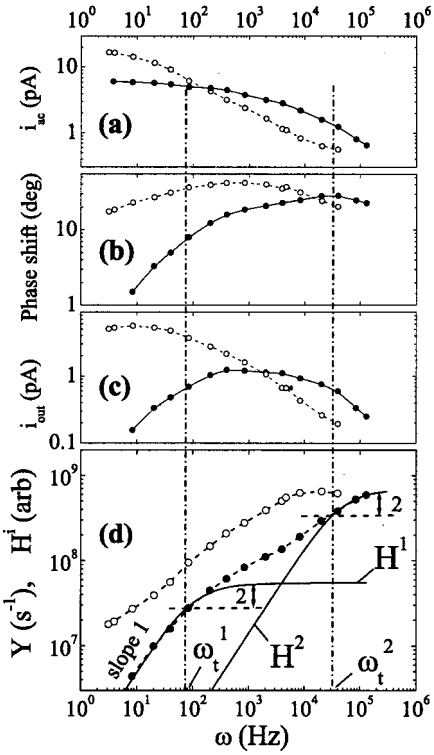

FIG. 2. Amplitude of MPC i_{ac} in (a), phase shift Φ in (b), amplitude of the out of phase MPC $i_{\rm out}$ in (c) and calculated values of Y term in (d) of our sample 1 as a function of angular frequency. Closed and open symbols obtained with a bias light intensity of 7×10^{12} and 5×10^{10} cm^{-2} s^{-1}, respectively. Vertical lines indicate the characteristic frequencies ω_t^1 and ω_t^2, while solid lines in (d) indicate the variation of the calculated weighting functions H^1, H^2 for the spectrum with the higher bias light level.

Figures 3–5 present the MPC data of undoped *a*-Si:H films that have been selected from the literature to be analyzed. Specifically, our experimental spectra published earlier[20] of i_{ac}, Φ, and $i_{\rm out}$ at 300 K from FRS spectroscopy of sample 2 deposited at ECD are shown in graphs (a), (b), and (c), respectively, of Fig. 3 for two bias light intensities. The respective experimental MPC spectra at 293 K of sample 3 from FRS spectroscopy published recently by Reynolds *et al.*[21] are presented in Figs. 4(a), 4(b), and 4(c) for two bias light intensities. Figure 5 presents experimental MPC data at $T=260$ K of sample 4 recorded by the BLS spectroscopy and published by Hattori *et al.*[22] The above authors have extracted the MPC signal S calculated from $S=(2/\pi kT)[G_{ac}e\mu\sin(\phi)/\sigma_{ac}+\omega]$ by means of experimental phase shift Φ and modulated photoconductivity σ_{ac} data recorded by varying the bias light level. This signal is shown in Fig. 5 as a function of the free electron density n for two angular modulation frequencies.

V. DATA ANALYSIS

A. Contributions from different kinds of defect states

It is observed that the above experimental spectra of phase shift and amplitude of the MPC exhibit crossing. This

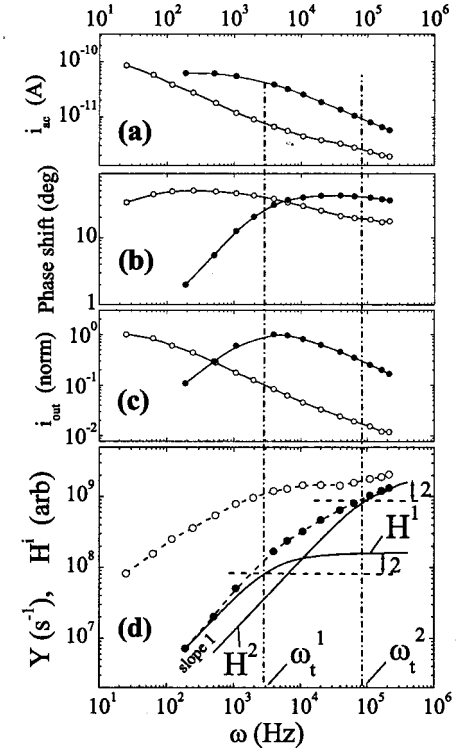

FIG. 3. Amplitude of MPC i_{ac} in (a), phase shift Φ in (b), amplitude of the out of phase MPC i_{out} in (c) of sample 2 from Ref. 10 and calculated values of Y term by means of Φ, i_{ac} in (d) as a function of angular frequency. Closed and open symbols obtained with a bias light intensity of 1×10^{13} and 1×10^{10} cm^{-2} s^{-1}, respectively. Vertical lines indicate the characteristic frequencies ω_t^1 and ω_t^2, while solid lines in (d) indicate the variation of the calculated weighting functions H^1, H^2 for the spectrum with the higher bias light level.

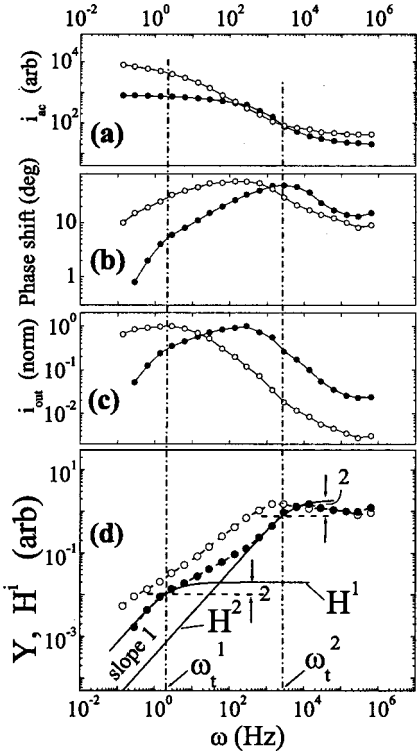

FIG. 4. Amplitude of MPC i_{ac} in (a), phase shift Φ in (b), amplitude of the out of phase MPC i_{out} in (c) of sample 3 from Ref. 21 and calculated values of Y term by means of Φ, i_{ac} in (d) as a function of angular frequency. Solid and open symbols obtained with a bias light generation rate of 4×10^{17} and 2×10^{15} cm^{-3} s^{-1}, respectively. Vertical lines indicate the characteristic frequencies ω_t^1 and ω_t^2, while solid lines in (d) indicate the variation of the calculated weighting functions H^1, H^2 for the spectrum with the higher bias light level.

crossing has been obtained also by simulation studies[19] when the electrons interact with various kinds of defect states. In this section, effective contributions to the MPC of various kinds of defect states with different capture coefficients for electrons are examined by analyzing the spectra of the Y term .

By taking that electrons predominate, the imaginary term Y, according to Sec. III, gives all the effective trapping rates $(\tau_b^i)^{-1}$ of electrons into the various kinds of defect states and provides all the information about the probing DOS. This term is calculated from Eq. (1) by means of the respective experimental Φ, i_{ac} data of the FRS spectroscopy, and it is plotted in Figs. 2(d), 3(d), and 4(d) as a function of angular modulation frequency ω. The right axis of Fig. 5 shows the Y term, which is directly related to the MPC signal S through the relation $Y=(\pi kT/2)S$. Apparently, in the respective spectra of the Y term in Figs. 2(d), 3(d), and 4(d) (solid symbols) obtained with the higher bias light level there are two drops at the frequencies ω_t^1 and ω_t^2 that are marked with vertical lines. Every drop in the Y term takes place at lower frequencies for lower bias light level, whereas the second drop of Y is not observed in all the spectra obtained with the lower bias light intensity (open symbols) because it is at frequencies below the detection limit of the lock in amplifier. In accordance, in each spectrum of Fig. 5 there are two drops of the Y term which are marked with arrows at the characteristic electron concentrations n^1 and n^2 for $\omega=62.8$ Hz (solid symbols) and to the higher electron concentrations $n^{1'}$ and $n^{2'}$ for $\omega=628$ Hz (open symbols).

The structure of Y in the above spectra is very similar to the ''staircaselike'' behavior of the simulated spectra of Fig. 1 where two kinds of defects were assumed. However, from Eq. (1) it is evident that the structures of Y spectra may originate either from the spectral variation of H^i, as in the simulation study of Fig. 1, or from a srtucture in $D^i(E)$. Therefore the ''staircaselike'' behavior alone cannot be taken as a proof that there are two kinds of defects in Y spectra. Hattori *et al.*[22] have analyzed the experimental data from the BLS spectroscopy as well. The two steps of the MPC signal in Fig. 5 were attributed[22] to the interaction of electrons with two kinds of defects. Their basic argument was that the probing energy levels, which were estimated from $E_b^i=kT\ln(c_n^i N_C/\omega)$, remain practically fixed in the energy gap and only the quasi-Fermi level E_t shifts below and above E_b^i by scanning at $n<n^i$ and $n>n^i$, respectively. In this way, the two steps in the MPC signal (Fig. 5) upon increasing n was thought to arise from a decrease of the effective contribution of the probing defect when the rising E_t crosses at $n=n^1$ and $n=n^2$ the respective fixed E_b^1 and E_b^2 levels. This was used

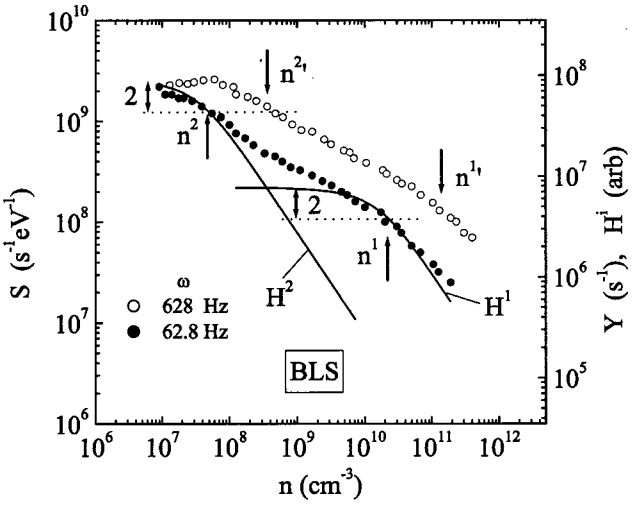

FIG. 5. MPC signal S (left axis) and *Y* term (right axis) as a function of the free electrons concentration *n* of sample 4 from Ref. 22 for two angular modulation frequencies. Arrows indicate the characteristic concentrations n^1, n^2 for $\omega=62.8$ Hz and $n^{1'}$, $n^{2'}$ for $\omega=628$ Hz. Solid lines indicate the respective variation of the weighting functions H^1, H^2 for the data with $\omega=62.8$ Hz.

to explain the experimental spectra in Fig. 5 and to determine the capture coeffcients of the two probing defects. However, the above expression, used by Hattori *et al.* to determine E_b^i, was derived from the emission-limited regime[14] and it cannot be applied also in the trapping-limited regime. Indeed, the more general expression of Eq. (2) indicates that the probing energy levels E_b^i shift along with the quasi-Fermi level E_t in the trapping-limited regime for $n>n^i$ and never become deeper than E_t.[19] Therefore the two steps of *Y* in Fig. 5 may not arise only from the drop of H function, but also from a possible ''staircaselike'' structure of the probing defect $D(E)$ distribution as the probing energy level shifts along with the quasi-Fermi level. Similarly, the two steps in the *Y* term from the FRS spectroscopy [Figs. 2(d), 3(d), and 4(d)] may arise from a ''staircaselike'' structure in the probing defect $D(E)$ distribution and not from the drop of the respective H^i functions.

It is then crucial to determine whether the structures in the *Y* spectra arise either (i) from a structure in the defect distribution or (ii) from the drop of H^i functions due to the interaction of electrons with two kinds of defect states. In the first possibility, if the two steps of *Y* arise from the spectral dependence of the probing defect distribution, then these steps should be observed at the same electron concentrations in BLS spectroscopy and at the same frequencies in FRS spectroscopy independent of the modulation frequency and bias light level, respectively. As it can be seen from the experimental spectra of *Y* this is not the case. In BLS spectroscopy the two steps of the *Y* spectra (Fig. 5) shift to higher electron concentrations by using a higher modulation frequency. In FRS spectroscopy the two steps of the *Y* spectra shift to higher frequencies by applying a higher bias light level. Therefore these two experimental facts rule out the first possibility. Moreover, the above behavior of the spectra obtained using a higher modulation frequency in BLS spectroscopy and that obtained when the samples are illuminated by a higher bias light level in FRS spectroscopy indicate the second possibility. Indeed, in the above cases, the two probing energy levels E_b^1 and E_b^2 (BLS spectroscopy) and the E_t level (FRS spectroscopy) shift to shallower levels in the energy gap so that the two steps of *Y* are expected to take place at two higher n^i and two higher ω_t^i values, respectively, as it is observed. This behavior of the Y spectra was also verified by simulations (not shown).

The above convince us that there is contribution mainly from two kinds of defects with different capture coefficients. The ''staircaselike'' behavior of *Y* arises then from the drop of H^1 and H^2 function supressing the effective contribution of the respective defect $D^1(E)$ and $D^2(E)$ and not from a spectral dependence of the probing defect distribution. Upon increasing *n* to n^2 and decreasing ω to ω_t^2 in BLS and FRS spectroscopy, respectively, the effective contribution of the one defect $D^2(E)$ with the higher capture coefficient decreases beacause its probing level E_b^2 comes closer to E_t. In this way, the effective contribution from the other defect $D^1(E)$, with the lower capture coefficient, which E_b^1 remains above E_t, is made evident. This is further verified by examining the relative variation of H^1 and H^2 functions calculated from Eq. (3) using the respective ω_t^i and n^i. These functions are also plotted in Figs. 2(d), 3(d), 4(d) and in Fig. 5 (solid lines). It can be seen that the variation of *Y* term in the transition region, around each ω_t^i and n^i, follows practically that of the respective weighting function H^i and so the *Y* term drops by a factor of 2 (double arrows). At this region, every probing energy level E_b^i, according to Eq. (2), remains practically at the respective quasi-Fermi level E_t and so every step of *Y* comes from the decrease of each H^i. Moreover, the variation of *Y* for $\omega<\omega_t^i$ follows the linear decrease of the respective weighting H^i function. This is more clearly shown in the spectrum of *Y* of Fig. 4 where the transtion frequencies have the larger difference so that the two steps of *Y* are well separated each other in the frequency domain. If there were additional contributions from other kinds of defects, then we should observe additional steps in the *Y* term. Thus possible contributions from additional defects should have probably a negligible effect to the imaginary term.

In addition, it was found that by adding the two H^i functions in Figs. 2–5 (solid lines), where their absolute magnitude was adjusted to fit *Y* at the respective step, the spectral shape of *Y* term is roughly obtained. This indicates that not only two defect states fit the data, but also that the two probing defect distributions are roughly uniform. This is also verified from the levelling off in the *Y* spectra that takes place for every $\omega>\omega_t^i$ and $n<n^i$. In this region, it is $H^i=1$ and the *Y* value gives the respective absolute probing $D^i(E)$. Every levelling off, and so the respective probing $D^i(E)$, were found to remain at about the same values for higher bias illumination (FRS) and higher frequency (BLS), shifting each step of *Y* and the respective probing energy levels E_b^i to shallower energies. This indicates that the two probing defect distributions have only a weak energy dependence.

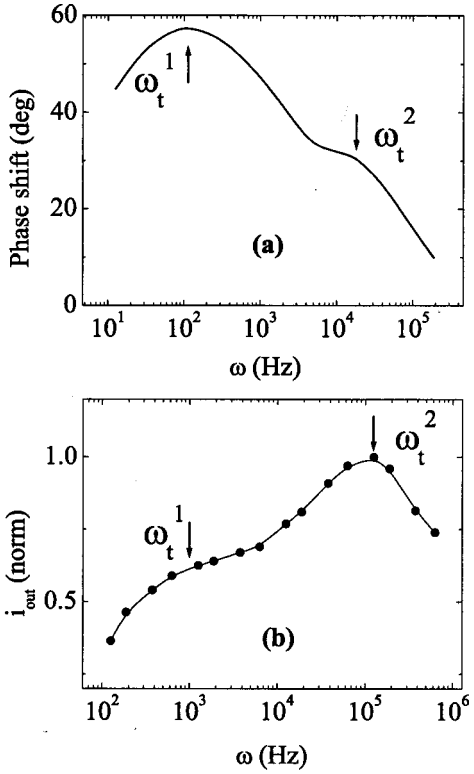

FIG. 6. Phase shift ϕ in (a) and out of phase MPC amplitude i_{out} spectra in (b) from Ref. 25 and 26, respectively. The frequency of the maximum and bump (arrows) indicate roughly the characteristic frequencies ω_t^1 and ω_t^2.

The presence of the two kinds of probing defect states in *a*-Si:H can be also manifested in the respective experimental spectra of Φ and i_{out} of FRS spectroscopy. As was shown previously with the aid of simulations,[19] every step of Y term in the transition region generates a maximum or bump in the calculated phase shift and out of phase MPC spectra, providing that these transition frequencies differ sufficiently in the frequency domain (about 2 orders of magnitude). Indeed, there is a maximum and pronounced bump in the spectra of Figs. 2(b), 2(c), 4(b), and 4(c) (solid symbols) at about the frequencies where the step of Y term is observed. These features were found to shift to higher frequencies upon rising the bias illumination level. A similar maximum and a pronounced bump appear also in the i_{out} and Φ spectra of *a*-Si:H from Refs. 25 and 26 that are included for comparison in Figs. 6(a) and 6(b), respectively. It must be emphasized that the bump in the above spectra becomes more pronounced in logarithmic scale, whereas in a linear scale it cannot be always clearly resolved [compare the phase shift spectrum of Fig. 4(b) with that of Fig. 5(b) of Ref. 21]. The absence of a pronounced bump in the spectra of Figs. 3(b) and 3(c) can be explained with the fact that the two transition frequencies of this case are relatively close to each other and so only a single broad maximum is observed. This was also confirmed from computer simulations[19] where only a single maximum was obtained in the calculated i_{out} and Φ spectra when the transition frequencies differ by less than 2 orders of magnitude in the frequency domain.

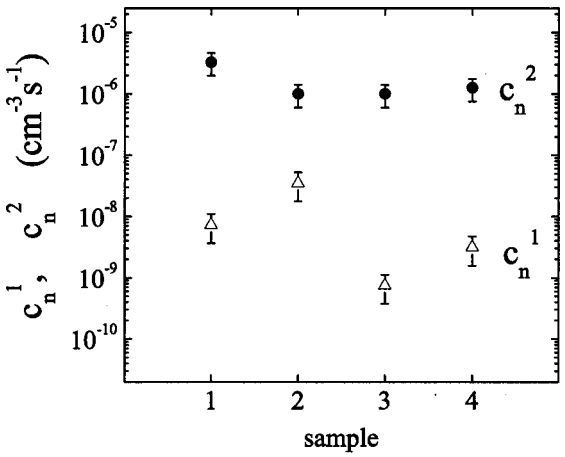

FIG. 7. Calculated capture coefficients c_n^1 (open symbols) and c_n^2 (solid symbols) for electrons of the $D^1(E)$ and $D^2(E)$ defects of the studied samples 1, 2, 3, and 4.

B. Capture coefficients

The absolute magnitude of the capture coefficients c_n^i of the probing defect states $D^i(E)$, which derived from the transition frequencies in Figs. 2, 3, and 4 and from the transition concentrations in Fig. 5, using Eqs. (5) and (6), respectively, by assuming that $\omega_t^i = nc_n^i$, $\omega = n^i c_n^i$, and $\mu = 10$ cm^2 V^{-1} s^{-1}, are summarized in Fig. 7. The values of the higher capture coefficient c_n^2 are about of the same order of magnitude (1×10^{-6} cm^{-3} s^{-1}) for all the samples in Figs. 2–5. The values of the lower capture coefficient c_n^1 in these samples scatter between 10^{-9} and 10^{-7} cm^{-3} s^{-1}, while the ratio c_n^2/c_n^1 is of the order of 10^2-10^3. A similar ratio of the capture coefficients is deduced from the transition frequencies corresponding to the bump and maximum of the spectra in Figs. 6(a) and 6(b) by concidering $c_n^2/c_n^1 \cong \omega_t^2/\omega_t^1$.

C. Defect distributions

As was shown in Sec. V A there is an effective contribution from two $D^1(E)$ and $D^2(E)$ distributions that dominate Y close to ω_t^1 and ω_t^2, respectively. In order to determine their energetic distributions it is required to define their probing energy levels. Figure 8 presents the probing energy levels E_b^1 and E_b^2 of the two defects as calculated from Eq. (2) for the experimantal data with the higher bias light level of Fig. 4 as a function of the modulation frequency. Similar graphs were obtained for the respective spectra of Figs. 2 and 3 (not shown). It can be seen that for every frequency in the spectral region of $\omega > \omega_t^1$ there are two different probing energy levels. Since $D^2(E)$ distribution dominates Y term at higher frequencies for $\omega \geqslant \omega_t^2$, this distribution is then extracted at E_t and above it from $D^2(E_b^2) = 2Y/(\pi kTc_n^2 H^2)$. Upon decreasing the frequency in the region of $\omega < \omega_t^2$, the probing energy level E_b^2 from Fig. 8 remains practically fixed at the quasi-Fermi level E_t, while E_b^1 shifts from shallower to deeper states up to E_t level. In this region, although there is a contribution from both defects, the contribution of $D^2(E)$

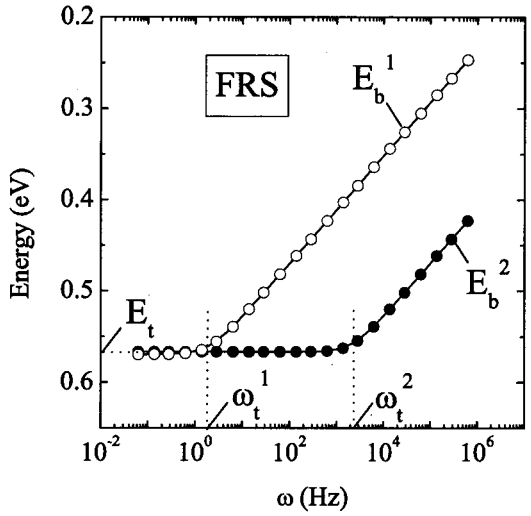

FIG. 8. Calculated probing energy levels E_b^1 and E_b^2 for the data from FRS spectroscopy of Fig. 4 with the higher bias light level as a function of angular modulation frequency.

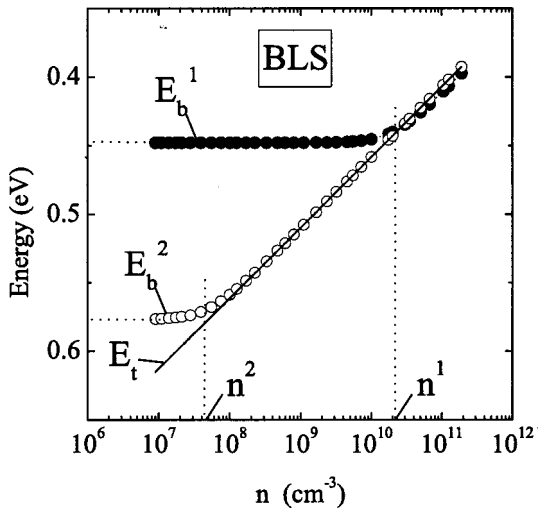

FIG. 9. Calculated probing energy levels E_b^1 and E_b^2 for the data from BLS spectroscopy of Fig. 5 with the lower modulation frequency as a function of free electrons concentration.

is $(\pi/2)H^2kTc_n^2D^2(E_t)$ and vanishes because of the drop of H^2 with decreasing ω. By subtracting this contribution from the Y term the remaining contribution $(\pi/2)H^1kTc_n^1D^1(E_b^1)$ is obtained from which the $D^1(E)$ is extracted at E_t and above it. The two calculated defect distributions are plotted in Fig. 10.

Since the probing energy level according to Eq. (2) may shift upon scanning in the region of $n>n^i$, it is then possible to extract also information about the two defect distributions from the experimental data of BLS spectroscopy. The two probing energy levels E_b^1 and E_b^2 of the $D^1(E)$ and $D^2(E)$, respectively, are demonstrated graphically in Fig. 9 for the experimantal data with the lower frequency of Fig. 5. It can be seen that the E_b^1 and E_b^2 shift along with the quasi-Fermi level E_t in the trapping-limited regime for $n>n^1$ and $n>n^2$, respectively. Therefore the variation of the MPC signal and of the imaginary term Y in the trapping-limited regime comes from the spectral dependence of the respective $D^i(E)$ and the drop of H^i. Only for $n<n^1$ and $n<n^2$ (emission-limited regime) the E_b^1 and E_b^2 remain fixed at 0.62 and 0.55 eV, respectively, above the E_t level and so both $D^i(E_b^i)$ and $H^i=1$ are fixed. Therefore for $n>n^1$ and $n>n^2$ it is possible to extract information about the two probing defect distributions $D^1(E)$ and $D^2(E)$, respectively. In this region, it can be seen from Fig. 5 that Y follows roughly the linear decrease of H^i suggesting only a weak energy dependence for the probing $D^i(E)$. As was shown in Sec. V A, the effective contribution of $D^1(E)$ and $D^2(E)$ dominates Y term of Fig. 5 near n^1 and n^2, respectively, because Y follows the variation of the respective H^1 and H^2 function. The absolute magnitude of $D^1(E)$ and its energetic distribution is extracted from $D^1(E_b^1)=2Y/(\pi kTc_n^1H^1)$ for $n\geqslant n^1$. In the region of $n<n^1$, E_b^1 is defined from the constant modulation frequency ω and according to Eq. (2) remains practically fixed at 0.44 eV well above E_t. The contribution of the $D^1(E)$ to Y term stays then at $(\pi/2)kTc_n^1D^1(E_b^1)$ as it is $H^1=1$. By subtracting this contribution from Y term the remaining contribution $(\pi/2)H^2kTc_n^2D^2(E_b^2)$ of the higher capture coefficient defects is obtained from which the $D^2(E)$ distribution is extracted.

The so derived $D^1(E)$ and $D^2(E)$ distributions from all the samples are plotted in Fig. 10 as a function of probing energy levels E_b^1 and E_b^2, respectively, as defined from Eq. (2). The DOS of sample 3 is in relative units and it has been plotted in Fig. 10 in order to fit with the absolute DOS of the rest samples. Figure 10 yields the surprising result that the defect distributions of all the samples agree very well despite that they come from different laboratories. They appear nearly flat as it is also predicted above by examining the spectral shape of Y. The absolute magnitude of $D^1(E)$ is about an order of magnitude higher than that of $D^2(E)$. Despite of the low defect density $D^2(E)$, these defects act as

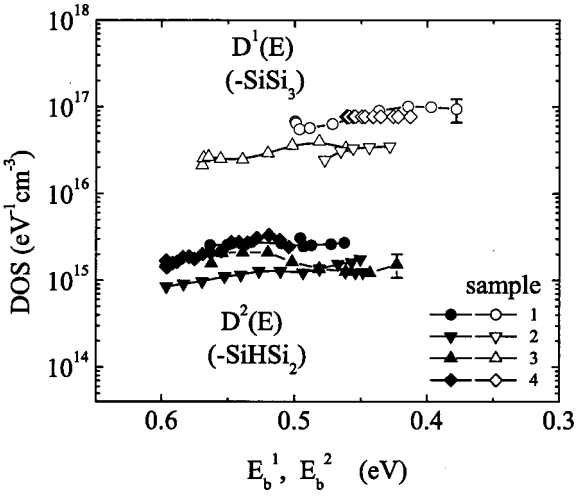

FIG. 10. Calculated defect densities of the two kinds of defects $D^1(E)$ (open symbols) and $D^2(E)$ (solid symbols) extracted from the Y term of graph (d) of Figs. 2–4 and Fig. 5 as a function of the respective probing energy level E_b^1 and E_b^2. Error bars have been put only in two data points for clarity.

relatively more effective electron capture centers because their capture coefficient is much higher than that of the $D^1(E)$ defects.

VI. DISCUSSION

The defect states with the higher capture coeficient could be assigned to positively charged defects D^+, whereas those with the lower capture coeficient could be assigned to neutral defects D^0. These defects dominate electron trapping and recombination above midgap, in qualitative agreement with the prediction of the defect pool model.[2,3] According to this model, electrons interact with the transition silicon dangling bond levels $D^{0/-}$ and $D^{+/0}$, corresponding to the above defect levels D^0 and D^+. If the $D^1(E)$ and $D^2(E)$ are assigned to D^0 and D^+, respectively, then it could be concluded from Fig. 10 that neutral defects appear in excess of the charged defects. However, this is not in agreement with the defect pool model, which in undoped samples predicts a charged defect density in excess of that of the neutral defects, which has been also confirmed experimentally.[5,27] In addition to this, the estimated 2–3 orders of magnitude difference in the capture coefficient of the probed defects of Fig. 7 cannot be attributed only to the charge-state of the dangling bonds. Indeed, the capture cross sections of the positively charged (σ_n^+) and neutral (σ_n^0) Si dangling bonds for electrons has been found from transient photoconductivity experiments[28,29] to differ only by about a factor of 5–30, namely, it is $\sigma_n^+/\sigma_n^0 = 5-30$.

In order to overcome the above difficulties and clarify the character of the probing defects, their local bonding configuration must be taken into account as well. Halpern[30] examined the role of the bonding configuration around the silicon dangling bonds in the carriers capture process. The above author pointed out that the vibration of hydrogen atom next to the silicon dangling bond will greatly enhanced its capture probability whatever the details of the multiphonon trapping process. Specifically, the trapping of a charge carrier by a dangling bond deep in the energy gap at about 0.6 eV involves the release of a considerable amount of energy which is assumed to involve multiphonon emission. By taking that the optical phonons in *a*-Si:H have an energy of around 0.06 eV, a carrier trapping by a dangling bond requires about 10 such phonons. On the other hand, the Si-H has a stretching mode of 2000 cm^{-1} or 0.25 eV. In this case, only 2–3 such phonons are required to absorb the energy released by carrier trapping into a dangling bond close to Si-H bond that appreciably increases the capture rate.

Therefore the defects with the lower capture coefficient (c_n^1) could be assigned to silicon dangling bonds with three backbonded silicon atoms ($-SiSi_3$), whereas the defects with the higher capture coefficient (c_n^2) to silicon dangling bonds where one backbond is substituted by hydrogen ($-SiHSi_2$). This interpretation is supported from the calculated difference in the magnitude of the respective multiphonon trapping rates. Specifically, in the weak coupling limit the transition rate is given by

$$W(E) = W_0[1+g(T)]^{n_{ph}} \exp[\gamma \Delta E/E], \qquad (7)$$

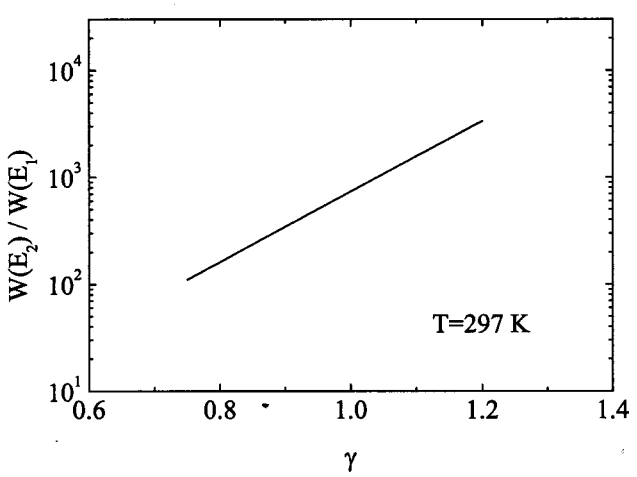

FIG. 11. Calculated ratio of $W(E_2)/W(E_1)$ at $T=297$ K for $\Delta E=0.6$ eV, $E_1=0.06$ eV and $E_2=0.25$ eV.

where $g(T)$ is the mean number of phonons of frequency ω, ΔE is the energy released by phonons of energy E, γ a constant close to unity that depends on the phonon coupling, and n_{ph} the number of phonons released, namely, it is $n_{ph} = \Delta E/E$. The difference in the magnitude of the rate $W(E)$ for $E_1=0.06$ eV and $E_2=0.25$ eV corresponding to the carriers trapping into dangling bonds in configuration ($-SiSi_3$) and ($-SiHSi_2$), respectively, is conciderably large and is sensitive to the magnitude of the phonon coupling (γ). This is demonstrated in Fig. 11 where it can be seen that when γ is ranging between 0.8 and 1.2 the ratio of $W(E_2)/W(E_1)$ calculated from Eq. (7) for $\Delta E=0.6$ eV and $T=297$ K varies by approximately 2–3 orders of magnitude, which is about the same with that measured for the ratio of c_n^2/c_n^1 of the studied samples of Fig. 7.

From the fact that the dangling bond density $D^2(E)$ from Fig. 10 is about an order of magnitude lower than the respective $D^1(E)$ density, it follows that there is a relatively lower density of dangling bonds next to Si-H bonds ($-SiHSi_2$) than that of the isolated dangling bonds ($-SiSi_3$). This is reasonable as one expects that very many of the dangling bonds are isolated from Si-H bonds and do not necessarily have Si-H bonds close to them. This conclusion is supported by pulsed electron spin resonance experiments in *a*-Si:H films of device quality. From these experiments it was deduced that hydrogen atoms are unlike to be situated at immediate neighborhood, at least, for the majority of dangling bonds indicating that they are formed mainly in the hydrogen-depleted region.[31]

Therefore the relative magnitudes of the defect densities $D^1(E)$, $D^2(E)$ and capture coefficients c_n^1, c_n^2 obtained from our analysis appear consistent with their assignment to isolated dangling bonds ($-SiSi_3$) and to dangling bonds with a Si-H backbond ($-SiHSi_2$), respectively. However, the charge state of the above probed defects cannot be extracted at present from our analysis.

The presence of various capture centers in the energy gap of *a*-Si:H with different capture coefficients for the carriers have been inferred also from the analysis of the mobility lifetime products of electrons and holes which deduced from

photoconductivity and diffusion length measurements.[32,33] It was suggested that the behavior of the above products upon changing temperature or bias illumination level can be reproduced by model simulations only if it was assumed that there are two kinds of capture centers with different capture coefficients. By increasing illumination level or by decreasing temperature, the simulations showed that the recombination is shifted from the centers of high capture coefficient, which assumed to be the dangling bonds, to low capture coefficient centers, which assumed to be the band tails. In this model, the high capture coefficients centers could be the $D^2(E)$ defects deduced from our analysis that have much higher capture coefficient than the rest centers. In a recent publication,[34] it was suggested that the above shift of the recombination channel may take place also from dangling bonds to discrete acceptorlike defects. It was proposed that these defects are induced by oxygen impurities below midgap and control the phototransport properties in *a*-Si:H rather the intrinsic defects. The defect states deduced from our analysis are above midgap and so they cannot be related to the above oxygen induced defects. In addition, the higher capture coefficient defects $D^2(E)$, which deduced from our analysis to dominate electron capture, cannot be related to oxygen or other impurities, such as nitrogen or carbon, induced defects. The phonon energies of the bonds of the above impurities in *a*-Si:H are comparable to those of Si-Si bonds. Therefore such possible impurity induced defects cannot provide according to our analysis the high capture rate of the above probed defects $D^2(E)$, which we attributed to the relatively higher phonon energies of the Si-H bond next to them.

VII. CONCLUSIONS

Our model analysis of the MPC is applied to the experimental spectra from FRS and BLS spectroscopy of glow discharge undoped *a*-Si:H films from different laboratories. The analysis of these data provides evidence that electrons interact with two kinds of defect states. Their capture coefficients differ by as much as 2–3 orders of magnitude, while their relative concentration differs by about an order of magnitude. We assign these defects to silicon dangling bonds with different back bond configurations. The defects with the lower capture coefficient and higher concentration are assigned to dangling bonds with three backbonded silicon atoms ($-SiSi_3$), whereas those with the higher capture coefficient and lower concentration to dangling bonds with a hydrogen backbond ($-SiHSi_2$).

*Electronic address: pkounavis@des.upatras.gr

[1] K. Winer, Phys. Rev. B **41**, 12 150 (1990).
[2] G. Schumm and G.H. Bauer, Philos. Mag. B **64**, 515 (1991).
[3] M.J. Powel and S.C. Dean, Phys. Rev. B **48**, 10 815 (1993).
[4] T. Shimizu, H. Kidoh, A. Morimoto, and M. Kumeda, Jpn. J. Appl. Phys., Part 1 **28**, 586 (1989).
[5] G. Schumm, W.B. Jackson, and R.A. Street, Phys. Rev. B **48**, 14198 (1993).
[6] W.B. Jackson and N.M. Amer, Phys. Rev. B **25**, 5559 (1982).
[7] M. Vanecek, J. Kocka, J. Stuchlik, and A. Triska, Solid State Commun. **39**, 1199 (1981).
[8] K. Pierz, B. Hilgenberg, H. Mell, and G. Weiser, J. Non-Cryst. Solids **97/98**, 91 (1987).
[9] J. D. Cohen J. Non-Cryst. Solids **114**, 381 (1989).
[10] G. Schumm, C.D. Abel, and G.H. Bauer J. Non-Cryst. Solids **137&138**, 351 (1991).
[11] M. Gunes and C. R. Wronski, J. Appl. Phys. **76**, 2260 (1994).
[12] M. Nesladek, G.J. Adriaenssens, and A.S. Volkov, J. Non-Cryst. Solids **137&138**, 443 (1991).
[13] Vanderhaghen and C. Longeaud, J. Non-Cryst. Solids **114**, 540 (1989).
[14] H. Oheda J. Appl. Phys. **52**, 6693 (1981).
[15] G. Schumm and G. Bauer, Phys. Rev. B **39**, 5311 (1989).
[16] R. Bruggemann, C. Main, J. Berkin, and S. Reynolds Philos. Mag. B **62**, 29 (1990).
[17] P. Kounavis and E. Mytilineou, J. Non-Cryst. Solids **137&138**, 955 (1991).
[18] J.P. Kleider and C. Longeaud, Solid State Phenom. **44/46**, 596 (1995).
[19] P. Kounavis, Phys. Rev. B **64**, 045204 (2001).
[20] P. Kounavis and E. Mytilineou, J. Non-Cryst. Solids **164/166**, 623 (1993).
[21] S. Reynolds, C. Main, D.P. Webb, and M.J. Rose Philos. Mag. B **80**, 547 (2000).
[22] K. Hattori, Y. Adachi, M. Anzai, H. Okamoto, and Y. Hamakawa, J. Appl. Phys. **76**, 2841 (1994).
[23] P. Kounavis and E. Mytilineou, J. Phys.: Condens. Matter **11**, 9105 (1999).
[24] D. Monroe, Phys. Rev. Lett. **54**, 146 (1985).
[25] P. Kounavis, N. Spiliopoulos, D. Mataras, and D. Rapakoulias, in *Proceedings of the* 13*th European Photovoltaic Solar Energy Conference, Nice, France*, edited by W. Freiesleden, W. Palx, A. Fssenbrick, and P. Helm (H. S. Stephens & Associates, Nice, France, 1995), Vol. I p. 288.
[26] D. Wagner, P. Irsigler, and D. Dunstan, Solid State Phys. **17**, 6793 (1984).
[27] T. Shimizu, M. Matsumoto, M. Yoshita, M. Iwami, A. Morimoto, and M. Kumeda, J. Non-Cryst. Solids **137&138**, 391 (1991).
[28] R. A. Street, Philos. Mag. B **49**, L15 (1984).
[29] W. E. Spear, A. C. Hourd, and S. Kinmond, J. Non-Cryst. Solids **77&78**, 607 (1985).
[30] V. Halpern, J. Non-Cryst. Solids **114**, 441 (1989).
[31] J. Isoya, S Yamasaka, H. Okushi, A. Matsuda, and K. Tanaka, Phys. Rev. B **47**, 7013 (1993).
[32] Y. Lubianiker, I Balberg, and L.F. Fonseca, Phys. Rev. B **55**, R15997 (1997).
[33] R. Rapaport, Y. Lubianiker and I Balberg, Appl. Phys. Lett. **72**, 103 (1998).
[34] I Balberg, R. Naidis, L.F. Fonseca, S.Z. Weisz, J.P. Conde, P. Alpuin, and V. Chu , Phys. Rev. B **63**, 113201 (2001).